Finite-Control-Set Model Predictive Control with Reduced Computational Burden in Cascaded H-Bridge Permanent Magnet Synchronous Motor Drives for EV Applications

1st Filippo Gemma
Electrical, Computer and Biomedical Engineering Dept
University of Pavia
Pavia, IT
filippo.gemma01@universitadipavia.it

2nd Jacopo Riccio
Power electronics, machines and control group
University of Nottingham
Nottingham, UK
Jacopo.Riccio2@nottingham.ac.uk

3rd Giulia Tresca
Electrical, Computer and Biomedical Engineering Dept
University of Pavia
Pavia, IT
giulia.tresca01@universitadipavia.it

4th Andrea Volpini
Electrical, Computer and Biomedical Engineering Dept
University of Pavia
Pavia, IT
andrea.volpini01@universitadipavia.it

5th Pericle Zanchetta
Electrical, Computer and Biomedical Engineering Dept
University of Pavia
Pavia, IT
pericle.zanchetta@unipv.it

***Abstract*—This article introduces an enhanced Finite-Control-Set Model Predictive Control (FCS-MPC) for Permanent Magnet Synchronous Motor (PMSM) drives powered by Multilevel Cascaded H-Bridge (CHB) inverters. The work focuses on reducing the algorithm computational complexity for torque control operations, ensuring State of Charge (SOC) balancing and reduced switching losses. The innovation lies in the utilization of adaptive Look-up Tables (LUTs) and an ad hoc objective function. Simulation results are provided to confirm the effectiveness of the proposed control approach in achieving accurate drive control with reduced switching frequency and enhanced SOC management. Additionally, the computational overhead of the proposed approach was measured on the target control platform to validate the reduction in computing complexity.**

***Index Terms*—Finite Control Set Model Predictive Control, Computational Burden Reduction, SOC Balancing, Switching Losses Reduction, Permanent Magnet Synchronous Motor**

I. Introduction

In Europe, the transportation sector is responsible for a significant portion, approximately one-third, of the total CO_2 emissions [1]. To address this issue and promote a greener environment, Battery Electric Vehicles (BEVs) with Permanent Magnet Synchronous Motor (PMSM) are considered the most promising solution. PMSMs inherent design with permanent magnets and synchronous operation ensures high efficiency and minimal losses, making them suitable for improving the driving experience by providing smooth and responsive performance. Moreover, PMSMs can operate over a wide range of speeds, providing optimal torque and power output across various driving conditions [2]. These attributes not only improve vehicle performance, but also help to meet severe efficiency and pollution regulations, which are precisely aligned with the long-term aims of electric transportation. However, the widespread adoption of BEVs faces several obstacles, including high costs and limited battery pack lifespan [3].

To overcome these challenges, Multilevel Converters (MCs) have emerged as promising electrical powertrain topologies [4]. MCs offer modularity, high-quality output voltage with reduced harmonic distortion and reduced device stress, providing fault tolerance and improved efficiency at partial loads [5]. Their inherent design adaptability seamlessly facilitates the growing trend of increased DC-link voltage in electrical power trains [6]. Additionally, MCs improve the battery management system, enhancing performance for BEVs by extending lifespan, enhancing safety, optimizing energy utilization and maintaining consistent power delivery [7]. The efficiency and power density of a Cascaded H-Bridge (CHB) inverter are comparable to those of an Insulated-Gate Bipolar Transistor (IGBT) and a Silicon-Carbide (SiC) 2-Level Voltage Inverter (2L-VSI), which is the standard topology for PMSM EV drives [8].

The modularity of the converters is further leveraged in a hierarchical distributed control architecture, consisting of primary control, secondary control, and battery State Of Charge (SOC) balancing control [9]. In PMSM drive systems fed by a CHB inverter, DC voltage unbalance can severely deteriorate performance [10]. A variable duty-cycle-based predictive control strategy has been proposed in [10] to overcome this issue. This strategy revises the duty cycles based on feedback from

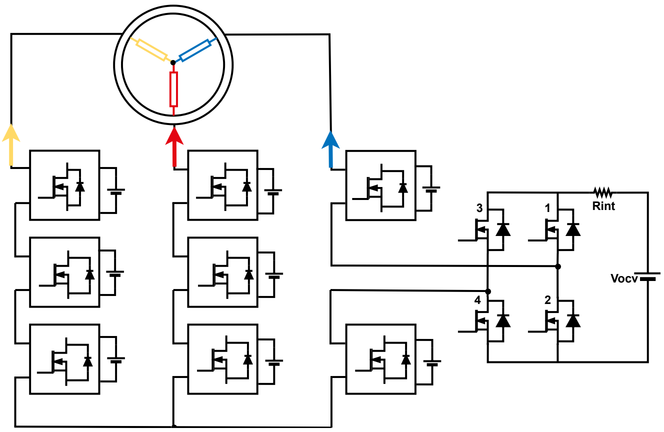

Fig. 1. Cascaded H-Bridge with simplified Li-Ion battery packs and PMSM motor.

the DC-link voltage of each cell, ensuring full utilization of each cell's DC source and improved steady-state performance under unbalanced conditions [10].

For MC applications, maintaining balance among the energy storage elements of the Sub-Modules (SM) is a common challenge. In applications where the battery pack is the main storage, such as motor drives, the SM voltage does not linearly relate to the overall battery SOC, complicating the balancing process. A method using nearest level control followed by sorting and selection based on the SOC of battery packs has been proposed in [11].

Recent research has focused on improving the performance of CHB through advanced control methods such as Finite Control Set Model Predictive Control (FCS-MPC) [12]. FCS-MPC solves an Integer Quadratic Optimal Control Problem (IQOCP) based on a state-space model over a predictive horizon [13], [14]. The control objectives are synthesized into a cost function, which allows for fulfilling several conflicting goals. However, solving the IQOCP and evaluating the cost function for MCs within a sampling interval poses significant challenges. The CHB topology increases the number of feasible Voltage Vectors (VVs) compared to traditional 2L-VSIs [15]. In [15], an offline optimization process reduces the computational complexity of FCS-MPC for the CHB. However, an online approach would improve the performance and guarantee real-time adjustments.

Furthermore, a fault-tolerant MPC control method combined with a novel power balancing approach has been developed for three-phase CHB inverters [16]. This method redistributes output voltage under switch open-fault and short-fault conditions using redundant voltage vectors and combination strategies. However, secondary balancing controls increase control complexity and underutilize the potential of multi-objective cost functions without reducing computational complexity.

This article introduces an enhanced FCS-MPC for CHB systems, depicted in Fig. 1. The proposed multi-objective cost function aims to eliminate steady-state errors, minimize device switching losses and balance the battery pack. By integrating these objectives into a unified cost function, hierarchical and secondary controls are eliminated, achieving comprehensive control objectives. Additionally, a novel time-varying online Look-Up Table (LUT) calculation ensures SOC balancing and computational efficiency, reducing switching combinations and overhead.

This paper is organised as follows. In Section II the model of the CHB-PMSM drive is described in details. In Section III, the proposed control method is presented. Simulation results are shown and commented in Section IV. Finally, the conclusions are reported in Section V.

TABLE I
PMSM AND LI-ION BATTERY PACK VALUES.

Variable	Symbol	Value	Unit
Stator Res.	R_s	0.47	Ω
Stator Ind.	$L_d = L_q$	4.15	mH
Rated Torque	T_{em}	15	Nm
Rated Speed	ω_m	3000	rpm
Max. Current	I_{max}	20	A
Rated Voltage	V_n	400	V
Pole Pairs	p	3	#
Perm. Flux Link.	ψ_m	0.255	Wb
Bat. capacity	C_n	104	Ah
Bat. Nom. Volt.	Vb_n	108.6	V

II. SYSTEM MODELLING

The powertrain system consists of Li-Ion battery packs, a Cascaded H-Bridge converter and a Permanent Magnet Synchronous Motor, as illustrated in Fig. 1.

A. PMSM and Batteries modelling

The parameters for the motor and batteries are provided in Tab. I. Each battery pack is modeled based on its SOC-dependent open-circuit voltage (V_{ocv}) and its equivalent internal resistance (R_{int}) [17]. V_{ocv} determines the battery's voltage characteristics under varying SOC, while R_{int} affects internal losses and voltage stability during operation.

The study has been conducted considering a motor model in dq coordinates synchronous with the PMSM rotor current [18], assuming: 1) linear magnetic characteristics and 2) ideal switching behavior of the converter. The defining equations of the PMSM in the dq frame can be expressed as [19]:

$$\begin{cases} v_d = R_s i_d + L_d \frac{di_d}{dt} - w_e i_q L_q \\ v_q = R_s i_q + L_q \frac{di_q}{dt} + w_e \left(i_d L_d + \psi_m \right) \end{cases} \tag{1}$$

$$T_{em} = \frac{3}{2} p \left(i_q \left(i_d L_d + \psi_m \right) - i_d i_q L_q \right) \tag{2}$$

where L_d, L_q, i_d, and i_q are the d- and q-axis inductances and currents, respectively, while ψ_m is the permanent magnet flux linkage. v_d and v_q are the dq stator voltages, whereas T_{em} is the electromagnetic torque. The symbol ω_e is the rotor electrical speed, R_s is the stator resistance, and p is the number of pole pairs.

TABLE II
VOLTAGE LEVEL AND SWITCHING STATE OF AN H-BRIDGE

Switching State				Output Voltage
S1	S2	S3	S4	
1	0	0	1	$+V_{bat}$
1	0	1	0	0
0	1	0	1	0
0	1	1	0	$-V_{bat}$

B. CHB modelling

Cascaded H-bridge multilevel inverters are composed of multiple units of single-phase H-bridge power cells. The H-bridge cells are normally connected in cascade on their AC side to achieve medium voltage operation and low harmonic distortion [17]. The CHB multilevel inverter requires a number of isolated DC supplies, each of which feeds an H-bridge power converter. In EV powertrain applications, each DC source corresponds to one battery pack unit. This cascade inverter makes EVs more accessible, safer and open wiring possible for most of the power systems because each low-voltage battery is isolated through switching devices. When switching devices are in an off-state, the leakage current is far less than the safety limit, which makes access possible to any point of the system [20]. With respect to the circuit diagram reported in Fig. 1, the output voltage of an H-bridge is presented in Tab. II and can be expressed as [21]:

$$V_{out} = V_{bat} * \left(\frac{1}{2}\left(S_1 + S_4\right) - \frac{1}{2}\left(S_2 + S_3\right) \right) \quad (3)$$

where V_{out} and V_{bat} represent the voltage output of the H-bridge and the battery pack voltage, respectively. The number of voltage levels (m) in a CHB inverter can be found from :

$$m = 2H + 1 \quad (4)$$

where H is the number of H-Bridge cells per phase leg, while the total number of active switches (N_{sw}) can be calculated as:

$$N_{sw} = 6\left(m - 1\right) \quad (5)$$

III. PROPOSED CONTROL

The block diagram of the proposed control method is depicted in Fig. 2. The speed of the Permanent Magnet Synchronous Motor is estimated using a position sensor. An outer speed loop based on a proportional-integral (PI) controller generates the torque reference, which is then converted to a current reference using a gain factor. The reference current is tracked via the proposed FCS-MPC. The Maximum Torque per Ampere (MTPA) and the Maximum Torque per Voltage (MTPV) characteristics of the machine are also considered to obtain the maximum torque for a given speed [22] with the minimum current magnitude.

The total number of switching state combinations for a three-phase CHB with 3 SM for phase can be calculated as $N_{swc} = 2^{2 \cdot N_{sub}} = 2^{18} = 262144$, where N_{sub} is the total number of H-bridge. Aimed at lowering the computational

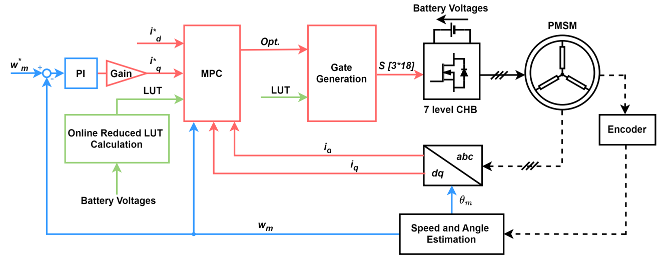

Fig. 2. Proposed control method (f= 20 kHz): (blue) PI speed control; (red) FCS-MPC current and balancing control; (green) LUT calculation.

burden, adaptive LUTs are implemented to reduce the number of possible switching states, as shown in Figs. 3(a), 3(c), and 3(e).

Different degrees of reduction are achieved by decreasing the switching combinations that result in specific voltages in the $\alpha\beta$ plane. Referring to Fig. 1 and Tab. II, only combinations with active $S1$ and $S3$ are considered to achieve battery bypass, omitting those with $S2$ and $S4$ conducting. Moreover multiple combinations are considered to achieve a desired output voltage in the LUT depicted in Fig. 3(a). When the system requires only one connected battery, three options can be considered, each with a different switching pattern. However, reducing the options to one (i.e. one switching pattern) minimizes the combinations, as depicted in Fig. 3(c). The offline switching pattern is initially determined by this reduction, but as battery voltages change during operation, the LUTs in the $\alpha\beta$ plane are updated online to predict current conditions accurately and ensure the active battery supports balancing. In conclusion, while the offline LUTs constrain the switching table, the online process selects which battery to use for balancing purposes.

Figs. 3(a), 3(c), and 3(e) display different combinations of redundancy for each potential VVs: each LUT ensures the application of all feasible VVs and minimizes the number of the required switching combinations.

Using one of the three LUT reductions significantly impacts the computational time of the MPC cost function. Specifically, the computational time for 3(a) is $1.66ms$ as depicted on Fig. 3(b), for 3(c) is $260\mu s$ as illustrated in Fig. 3(d), and for 3(e) is $96.4\mu s$ as shown in Fig. 3(f). These times (i.e. cost function times) were measured and verified using an oscilloscope and tested on the uCube control platform with the first optimization method [23]. The reduction in computational time corresponds directly to the decrease in the number of switching state combinations, thereby optimizing and speeding up the control.

The implementation of an online LUT calculation ensures active battery balancing during the motoring phase. In this work, the LUT depicted in Fig. 3(c) is selected, which ensures balancing and computational reduction and considers an additional term in the MPC cost function to minimize converter switching losses.

The FCS-MPC enables the formulation of the optimization problem, featuring the inclusion of constraints on SOC

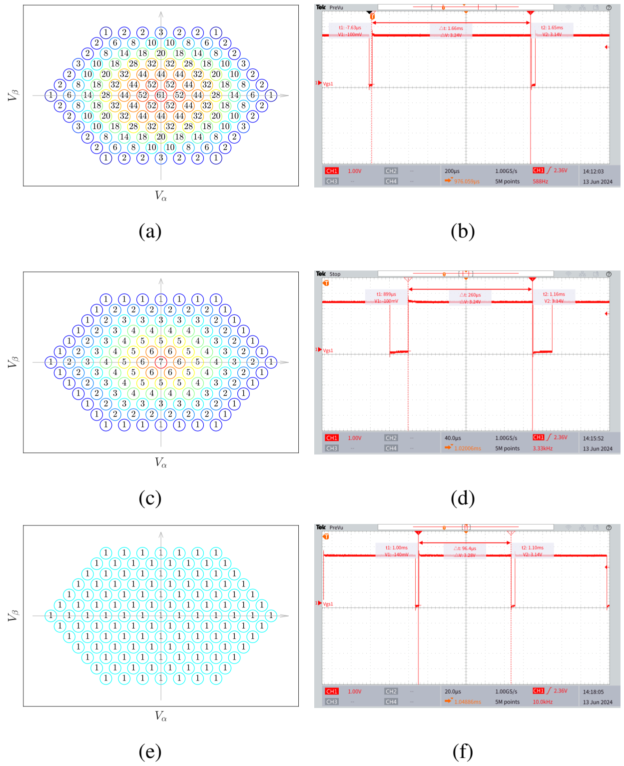

Fig. 3. LUTs with different gradients of reduction and respective calculation times of the cost function: (a) 2197 feasible VVs; (b) 2197 feasible VVs computational time; (c) 343 feasible VVs; (d) 343 feasible VVs computational time; (e) 127 feasible VVs; (f) 127 feasible VVs computational time.

balancing and switching loss reduction. This is achieved while concurrently reducing computational costs through the evaluation of fewer combinations, assured by the utilization of the LUT.

The cost function employed in FCS-MPC, denoted as $g(n)$, is defined as follows:

$$g(n) = \left\| \mathbf{i_{d,q}}^* - \mathbf{i_{d,q}}^{k+1}(n) + W_{i_{d,q}} T_s \left(\sum_{j=0}^{m} \mathbf{i_{d,q\ err}}^{k-j} \right) \right\|_2^2 + \lambda_1 \Delta SOC^{k+1}(n) + \lambda_2 \Delta U(n) \tag{6}$$

The equation represents the squared two-norm of the difference between the current references $i^*_{d,q}$ and the predicted currents $i^{k+1}_{d,q}(n)$. The current predictions are based on the simplified PMSM drive model, discretized using the forward Euler approximation as follows:

$$i_d^{k+1}(n) = i_d^k + \frac{T_s}{L_d} \left(v_d(n) - R_s i_d^k + w_e i_q^k L_q \right) \tag{7a}$$

$$i_q^{k+1}(n) = i_q^k + \frac{T_s}{L_q} \left(v_q(n) - R_s i_q^k - w_e \left(i_d^k L_d + \psi_m \right) \right) \tag{7b}$$

n represents the index for the possible switching combination (e.g., 343 for the specified LUT). T_s denotes the control sample time ($T_s = 5e^{-5}$ s). The term $W_{i_{d,q}} T_s \left(\sum_{j=0}^{m} i_{d,q\ err}^{k-j} \right)$ incorporates an integral action aimed at increasing the system robustness [24, 25]. The term $\lambda_1 \Delta SOC^{k+1}(n)$ imposes constraints, on the maximum predicted difference in the State of Charge. For each iteration, the SOC prediction for each battery pack is computed using the Coulomb counting method [26]:

$$SOC^{k+1}(n) = SOC^k - \frac{T_s * |I_{phase}|}{3600 * C_n} \tag{8}$$

The difference between the maximum and minimum SOC predictions among the battery pack provides $\Delta SOC^{k+1}(n)$ for each switching combination. A higher value of $\Delta SOC^{k+1}(n)$ penalizes the cost function, indicating greater SOC variation among battery packs at time step $k+1$, not benefiting the balance of the battery pack. The final component of the cost function, $\lambda_2 \Delta U(n)$, aims to minimize switching losses and is defined as follows:

$$\Delta U(n) = \frac{n_c(n)}{\text{Total number of switches}} \tag{9}$$

where $n_c(n)$ represents the number of switching commutations that occur at time step $k+1$ compared to time step k, while the total number of switches denotes the total half-bridge of the topology, penalizing switching actions will reduce the frequency of converter switching events and the associated losses.

Finally, the actuating command n that minimizes (6) is selected for the next time step to control the system at the desired operating point effectively.

TABLE III
STATE OF CHARGE STARTING CONDITIONS FOR BATTERY PACK.

	Value	Unit
Phase A	0.90	p.u.
	0.93	p.u.
	0.87	p.u.
Phase B	0.88	p.u.
	0.86	p.u.
	0.95	p.u.
Phase C	0.90	p.u.
	0.91	p.u.
	0.89	p.u.

IV. SIMULATIONS RESULTS

The simulation tests have been conducted using Simulink, MATLAB. The aim of the simulations involves controlling the torque and speed of the PMSM while ensuring active balancing of the battery packs during motoring. The proposed control is tested for the reduced LUT depicted in Fig. 3(c) and for three significant operating points: machine base speed (i.e. $\omega_b = 3000$ rpm), first field-weakening speed (i.e. $\omega_{fw} = 4000$ rpm) and second field-weakening speed (i.e. $\omega_{sw} = 4500$ rpm). The starting SOCs conditions are listed in Tab. III. A comparison between the proposed FCS-MPC and the state-of-the-art PI control technique for current control and battery pack balancing in MCs [27] is presented in Fig. 4, while a

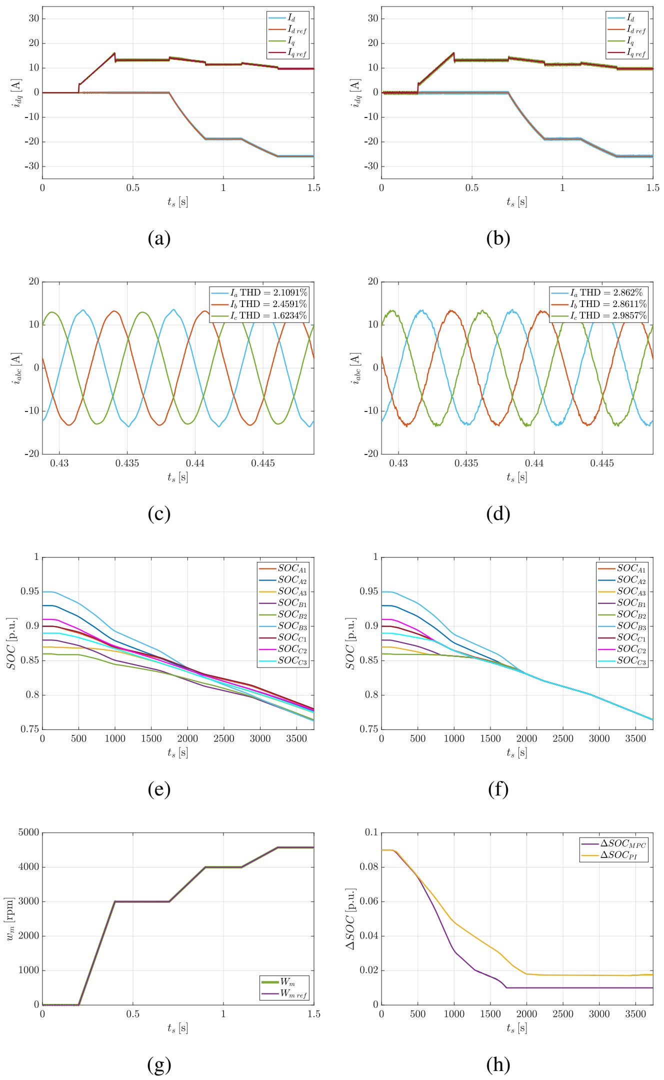

Fig. 4. Simulation results PI vs FCS-MPC control: (a) d- and q-current PI control; (b) d- and q-current FCS-MPC control; (c) I_a, I_b and I_c current PI control; (d) I_a, I_b and I_c current FCS-MPC control; (e) SOCs behaviour during a motoring cycle with PI control; (f) SOCs behaviour during a motoring cycle with FCS-MPC control; (g) w_m control for PI and FCS-MPC; (h) ΔSOC maximum of the battery pack.

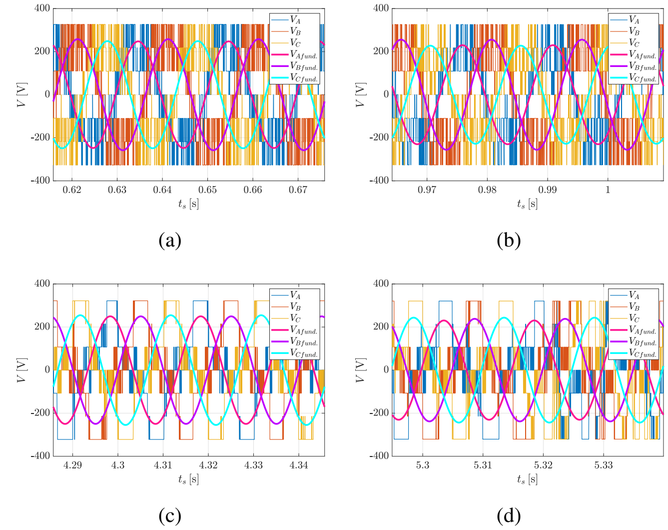

Fig. 5. Output voltages with their 1^{st} fundamental harmonic from the CHB going into the motor:(a) Phase voltages at 3000 RPM and SOC unbalanced; (b) Phase voltages at 4000 RPM and SOC unbalanced; (c) Phase voltages at 3000 RPM and SOC balanced; (d) Phase voltages at 4000 RPM and SOC balanced.

comparison with different values of λ_1 and λ_2 is illustrated in Fig. 6.

Both in the proposed FCS-MPC and the state-of-the-art PI control, it is noted that in all three speed regions, the controlled variables follow the reference signal, as depicted in Fig. 4(a) and Fig. 4(b) for the d- and q-current components and in Fig. 4(g) for the machine rotational speed. Additionally, it is noted that the current ripple is higher when using FCS-MPC, as shown in Fig. 4(d) concerning Fig. 4(c) for the PI technique. However, with the proposed control method, all currents exhibit the same Total Harmonic Distortion (THD), while in the state-of-the-art method, the THD gap between the phases is higher, due to the SOC balancing that is performed outside the main control. This unbalanced behavior in a single phase can lead to unbalanced deterioration of the machine under testing [28].

Figs. 4(e) and 4(f) demonstrate how active balancing among the battery packs of the powertrain can be ensured. Starting from the same unbalanced condition, presented in Tab. III, the unbalance is eliminated during the motoring operation for both cases. In the case of FCS-MPC, the balancing state is reached in a shorter time, exactly 400 s earlier, as shown in Fig. 4(h). Compared to the state-of-the-art method, the proposed method also achieves a lower total battery pack imbalance, as shown in Fig. 4(h). Additionally, unlike conventional balancing methods, the MPC-FCS does not require extra controllers such as parallel PIs or duty cycle modifications.

Figs.5(a) and 5(b) show the output voltages of the converter and their respective 1^{st} harmonics at two operating points when the SOCs are unbalanced: at base speed (3000 rpm) and in the first flux-weakening region (4000 rpm). The higher peak of the 1^{st} harmonic of V_B is due to the unbalanced SOC conditions under which the drive is operating. Figs. 5(c) and 5(d) present the CHB output voltages under the same operating conditions but with balanced SOC. When the batteries' SOC are balanced, the 1^{st} harmonics have the same amplitude, indicating that the different peaks observed in the first case are due to the SOC imbalance in the battery pack.

The total harmonic distortion of the output voltage is significantly improved compared to the state-of-the-art benchmark [27], highlighting that CHB inverters offer an optimal choice for improving efficiency, reducing harmonic content and meeting the high voltage demands of modern electric power systems.

Considering different weights, λ_1 and λ_2, in the cost function yields different outcomes. Consequently, depending on the objective and operating conditions, (6) can be modified to

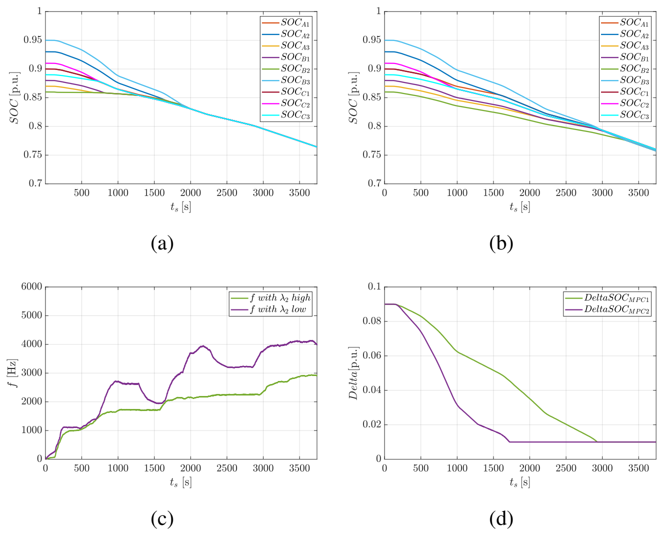

Fig. 6. Simulation results with different weighting factors, λ_1 and λ_2, in (6): (a) SOCs behaviour during a motoring cycle with $\lambda_1 = 6.2e^1$ and $\lambda_2 = 3.5e^{-1}$; (b) SOCs behaviour during a motoring cycle with $\lambda_1 = 4.81e^1$ and $\lambda_2 = 5.53e^{-1}$; (c) Switching frequency behaviour during a motoring cycle; (d) $\Delta SOCs$ maximum of the battery pack.

achieve the desired results, such as decreasing the balancing time or reducing the switching frequency. Decreasing the value of λ_1 increases the time required for balancing, as shown in Figs. 6(a) and 6(b). However, by increasing the balancing time, the term λ_2 can be increased, leading to a decrease in the equivalent switching frequency, as shown in Fig. 6(c), and consequently reducing switching losses.Therefore, analyzing the results presented in Fig. 6, it is evident that based on the application and targets, the balancing time can be accelerated by increasing the switching frequency or, conversely, switching losses can be reduced by increasing the balancing time.

V. Conclusions

A reduced computational burden FCS-MPC is here proposed. The algorithmintegrates the torque control and the SOC management during the motoring of an EV-based PMSM drive system powered by a CHB inverter. In addition to demonstrating the feasibility of the control through simulation, the different calculation times of the proposed reduced LUTs were experimentally calculated, highlighting how the adoption of a LUT can actively impact the practical feasibility and implementation of the suggested technique.

The simulation results demonstrate the effectiveness of the suggested control for accurate motor control, reduced switching frequency and losses and balanced SOCs. Several scenarios were considered for comparisons with state-of-the-art balancing methods, highlighting that compared to classical methods, the proposed FCS-MPC allows for more accurate and faster balancing. Moreover, the flexibility of the objective function allows for varying the control behavior based on the application, enabling either reduced switching losses or shorter balancing times.

VI. Acknowledgement

This work was supported by the Clean Sky 2 Joint Undertaking through the European Union's Horizon 2020 Research and Innovation Program under Grant 807081 and Grant 821023.

References

[1] V. V. Georgatzi, Y. Stamboulis, and A. Vetsikas, "Examining the determinants of co2 emissions caused by the transport sector: Empirical evidence from 12 european countries," *Economic Analysis and Policy*, vol. 65, pp. 11–20, 2020.

[2] L. Zhong, M. Rahman, W. Hu, and K. Lim, "Analysis of direct torque control in permanent magnet synchronous motor drives," *IEEE Transactions on Power Electronics*, vol. 12, no. 3, pp. 528–536, 1997.

[3] E. A. Grunditz and T. Thiringer, "Performance analysis of current bevs based on a comprehensive review of specifications," *IEEE Transactions on Transportation Electrification*, vol. 2, no. 3, pp. 270–289, 2016.

[4] D. Ronanki and S. S. Williamson, "Modular multilevel converters for transportation electrification: Challenges and opportunities," *IEEE Transactions on Transportation Electrification*, vol. 4, no. 2, pp. 399–407, 2018.

[5] G. Tresca, A. Formentini, J. Riccio, N. Anglani, and P. Zanchetta, "A reconfigurable cascaded multilevel converter for ev powertrain," *IEEE Transactions on Industry Applications*, vol. 60, no. 2, pp. 3332–3344, 2024.

[6] A. Poorfakhraei, M. Narimani, and A. Emadi, "A review of multilevel inverter topologies in electric vehicles: Current status and future trends," *IEEE Open Journal of Power Electronics*, vol. 2, pp. 155–170, 2021.

[7] F. Gemma, G. Tresca, S. R. Di Salvo, A. Formentini, and P. Zanchetta, "A novel charging approach to temperature and state of charge management in bev," pp. 2706–2712, 2023.

[8] F. Chang, O. Ilina, M. Lienkamp, and L. Voss, "Improving the overall efficiency of automotive inverters using a multilevel converter composed of low voltage si mosfets," *IEEE Transactions on Power Electronics*, vol. 34, no. 4, pp. 3586–3602, 2019.

[9] B. Xu, H. Tu, Y. Du, H. Yu, H. Liang, and S. Lukic, "A distributed control architecture for cascaded h-bridge converter with integrated battery energy storage," *IEEE Transactions on Industry Applications*, vol. 57, no. 1, pp. 845–856, 2021.

[10] H. Yao, Y. Yan, Y. Cao, P. Song, and T. Shi, "A variable duty cycle-based predictive control for pmsm fed by cascaded h-bridge inverter," *IEEE Journal of Emerging and Selected Topics in Power Electronics*, vol. 10, no. 4, pp. 4195–4206, 2022.

[11] L. Mathe, P. Dan Burlacu, E. Schaltz, and R. Teodorescu, "Battery pack state of charge balancing algorithm for cascaded h-bridge multilevel converters," pp. 1–6, 2016.

[12] P. Cortés, A. Wilson, S. Kouro, J. Rodriguez, and H. Abu-Rub, "Model predictive control of multilevel cascaded h-

bridge inverters," *IEEE Transactions on Industrial Electronics*, vol. 57, no. 8, pp. 2691–2699, 2010.

[13] P. Karamanakos and T. Geyer, "Guidelines for the design of finite control set model predictive controllers," *IEEE Transactions on Power Electronics*, vol. 35, no. 7, pp. 7434–7450, 2020.

[14] P. Karamanakos, E. Liegmann, T. Geyer, and R. Kennel, "Model predictive control of power electronic systems: Methods, results, and challenges," *IEEE Open Journal of Industry Applications*, vol. 1, pp. 95–114, 2020.

[15] G. Scaglione, C. Nevoloso, G. Schettino, A. O. Di Tommaso, and R. Miceli, "A novel multi-objective finite control set model predictive control for ipmsm drive fed by a five-level cascaded h-bridge inverter," *IEEE Journal of Emerging and Selected Topics in Power Electronics*, pp. 1–1, 2024.

[16] X. Wang, Y. Zhao, R. Yang, W. Hu, and T. Zou, "Model predictive-based fault-tolerant and power balancing control for cascaded h-bridge inverter," *IEEE Transactions on Power Electronics*, vol. 39, no. 5, pp. 5257–5270, 2024.

[17] F. Gemma, G. Tresca, A. Formentini, and P. Zanchetta, "Balanced charging algorithm for chb in an ev powertrain," *Energies*, vol. 16, no. 14, 2023. [Online]. Available: https://www.mdpi.com/1996-1073/16/14/5565

[18] E. Zerdali and P. Wheeler, "Model-free simplified predictive current control of pmsm drive with ultra-local model-based ekf," in *2021 3rd Global Power, Energy and Communication Conference (GPECOM)*, 2021, pp. 62–66.

[19] E. Zerdali, M. Rivera, P. Wheeler, and S. Toledo, "Predictive direct speed control of pmsm without weighting factors," pp. 1–6, 2023.

[20] L. Tolbert, F. Peng, and T. Habetler, "Multilevel inverters for electric vehicle applications," in *Power Electronics in Transportation (Cat. No.98TH8349)*, 1998, pp. 79–84.

[21] B. Wu and M. Narimani, *Cascaded H-Bridge Multilevel Inverters*, 2017, pp. 119–141.

[22] J. Riccio, L. Rovere, S. Odhano, M. Di Nardo, and P. Zanchetta, "Model-predictive control of open-end winding synchronous reluctance motor drives," in *2022 IEEE Energy Conversion Congress and Exposition (ECCE)*, 2022, pp. 1–8.

[23] A. Galassini, G. Lo Calzo, A. Formentini, C. Gerada, P. Zanchetta, and A. Costabeber, "ucube: Control platform for power electronics," pp. 216–221, 2017.

[24] J. Riccio, P. Karamanakos, S. Odhano, M. Tang, M. D. Nardo, and P. Zanchetta, "Direct model predictive control of synchronous reluctance motor drives," *IEEE Transactions on Industry Applications*, vol. 59, no. 1, pp. 1054–1063, 2023.

[25] J. Riccio, P. Karamanakos, S. Odhano, M. Tang, M. Di Nardo, and P. Zanchetta, "A direct model predictive control strategy for high-performance synchronous reluctance motor drives," in *2021 IEEE Energy Conversion Congress and Exposition (ECCE)*, 2021, pp. 4704–4710.

[26] K. S. Ng, C.-S. Moo, Y.-P. Chen, and Y.-C. Hsieh, "Enhanced coulomb counting method for estimating state-of-charge and state-of-health of lithium-ion batteries," *Applied Energy*, vol. 86, no. 9, pp. 1506–1511, 2009.

[27] M. Quraan, T. Yeo, and P. Tricoli, "Design and control of modular multilevel converters for battery electric vehicles," *IEEE Transactions on Power Electronics*, vol. 31, no. 1, pp. 507–517, 2016.

[28] A. Bonnett and G. Soukup, "Cause and analysis of stator and rotor failures in three-phase squirrel-cage induction motors," *IEEE Transactions on Industry Applications*, vol. 28, no. 4, pp. 921–937, 1992.